



1 Volcanic SO₂ Effective Layer Height Retrieval for OMI Using a
2 Machine Learning Approach

3 Nikita M. Fedkin¹, Can Li², Nickolay A. Krotkov², Pascal Hedelt³, Diego G. Loyola³, Russell R.
4 Dickerson¹, Robert Spurr⁴

5 1: Department of Atmospheric and Oceanic Science, University of Maryland, College Park, MD, USA

6 2: NASA Goddard Space Flight Center, Greenbelt, MD 20771, USA

7 3: German Aerospace Center (DLR), Remote Sensing Technology Institute (IMF), Oberpfaffenhofen, Germany

8 4: RT Solutions Inc., Cambridge, MA, USA

9

10 *Correspondence to:* Nikita M. Fedkin (nfedkin@umd.edu)

11

12 **Abstract.** Information about the height and loading of sulfur dioxide (SO₂) plumes from
13 volcanic eruptions is crucial for aviation safety and for assessing the effect of sulfate aerosols on
14 climate. While SO₂ layer height has been successfully retrieved from backscattered Earthshine
15 ultraviolet (UV) radiances measured by the Ozone Monitoring Instrument (OMI), previously
16 demonstrated techniques are computationally intensive and not suitable for near real-time
17 applications. In this study, we introduce a new OMI algorithm for fast retrievals of effective
18 volcanic SO₂ layer height. We apply the Full Physics Inverse Learning Machine (FP_ILM)
19 algorithm to OMI radiances in the spectral range of 310-330 nm. This approach consists of a
20 training phase that utilizes extensive radiative transfer calculations to generate a large dataset of
21 synthetic radiance spectra for geophysical parameters representing the OMI measurement
22 conditions. The principal components of the spectra from this dataset in addition to a few
23 geophysical parameters are used to train a neural network to solve the inverse problem and
24 predict the SO₂ layer height. This is followed by applying the trained inverse model to real OMI
25 measurements to retrieve the effective SO₂ plume heights. The algorithm has been tested on
26 several major eruptions during the OMI data record. The results for the 2008 Kasatochi, 2014
27 Kelud, 2015 Calbuco, and 2019 Raikoke eruption cases are presented here and compared with
28 volcanic plume heights estimated with other satellite sensors. For the most part, OMI-retrieved
29 effective SO₂ heights agree well with the lidar measurements of aerosol layer height from Cloud-
30 Aerosol Lidar and Infrared Pathfinder Satellite Observations (CALIPSO) and thermal infrared
31 retrievals of SO₂ heights from the infrared atmospheric sounding interferometer (IASI). The
32 errors in OMI retrieved SO₂ heights are estimated to be 1-1.5 km for plumes with relatively large
33 SO₂ signals (> 40 DU). The algorithm is very fast and retrieves plume height in less than 10 min
34 for an entire OMI orbit. This approach offers a promising prospect of using physics-based
35 machine learning applications to other instruments.



36

37

38 **1 Introduction**

39

40 The observation and tracking of emissions from volcanic eruptions are crucial for both air traffic
41 safety and for assessing climate forcing impacts from volcanic sulfate aerosols. In the last 10
42 years, volcanoes have emitted roughly 20-25 million metric tons of sulfur dioxide (SO₂) per year
43 through passive degassing (Carn et al, 2017). Explosive volcanic eruptions, however, can
44 additionally release large SO₂ amounts high into the atmosphere. SO₂ can be converted to sulfate
45 aerosols within 2-3 days in the troposphere (Lee et al., 2011) and within a few weeks in the
46 lower stratosphere (von Glasow et al., 2009, Krotkov et al., 2010). Sulfate aerosols are known to
47 have a cooling effect on climate, especially if an SO₂ plume is injected into the lower
48 stratosphere and remains there for longer periods of time. This is demonstrated by significant
49 eruptions such as Mt. Pinatubo in 1991 that temporarily reduced global temperatures by up to
50 0.5°C (McCormick et al, 1995). Aside from releasing SO₂, volcanoes also emit large amounts of
51 ash into the atmosphere which can have adverse impacts on air travel. Ash from volcanic plumes
52 can often interfere with flight paths, greatly reduce visibility near the ground, and cause damage
53 to the aircraft including engine failure (Carn et al., 2009). In addition, SO₂ causes sulfidation in
54 the engines, an effect that can reduce their lifetimes in the long term. From 1953 to 2009, over
55 120 aviation incidents involving volcanic activity were reported, with roughly 80 of them
56 involving serious damage to the airframe or engine (Guffanti et al., 2010). There is also the
57 possibility of highly concentrated volcanic SO₂ plumes producing acidic aerosols which can
58 cause irritation of the eyes, nose and respiratory airways of occupants inside airplanes (Schmidt
59 et al., 2014). In many cases SO₂ and ash are often collocated, thus making estimates of SO₂ layer
60 height very useful for aviation hazard mitigation and volcanic plume forecasting. Lastly, the
61 accurate determination of SO₂ height can ideally aid in producing accurate SO₂ VCD estimates
62 given that those retrievals typically use a fixed *a priori* vertical distribution of SO₂ in the absence
63 of additional information on SO₂ height.

64 With remote sensing, these volcanic plumes can be regularly observed from space. In
65 particular, hyperspectral spectrometers such as the Ozone Monitoring Instrument (OMI),
66 GOME-2, OMPS, TROPOMI and others, have provided frequent and increasingly accurate
67 observations of global SO₂ amounts, through retrieval algorithms from backscattered radiance



68 measurements. The OMI instrument, a Dutch-Finish contribution to the NASA Aura satellite,
69 has been operational since 2004. OMI has 60 cross track positions (rows) and has a $13 \times 24 \text{ km}^2$
70 spatial resolution at the nadir position (Levelt et al., 2006). The instrument uses two UV channels
71 and one visible channel to measure backscattered radiances from the Earth's atmosphere. In
72 general, SO_2 slant column amounts are retrieved from these measurements through the
73 differential optical absorption spectroscopy (DOAS) technique and then converted to vertical
74 columns using Air Mass Factors (AMFs). The 310.5-340 nm range in OMI's UV2 channel is
75 used in retrieving SO_2 , with focus on the 310.8 and 313 nm wavelengths. The band residual
76 algorithm (Krotkov et al., 2006) and the Linear Fit (LF) algorithm (Yang et al., 2007) were first
77 used as the OMI operational algorithms for retrieving planetary boundary layer (PBL) SO_2 and
78 volcanic SO_2 vertical column densities (VCDs) respectively. These were replaced with the
79 principal component analysis (PCA) based algorithm (Li et al., 2013) which retrieves SO_2
80 amounts directly from spectral radiance measurements. The same technique was also applied to
81 OMI volcanic SO_2 retrievals (Li et al., 2017). This data-driven approach does not rely on
82 extensive radiative transfer modeling and has led to reduced biases and significant improvements
83 (Fioletov et al., 2015). For volcanic retrievals, algorithms still have uncertainties in SO_2 mass in
84 volcanic plumes, especially in the presence of relatively larger errors in the assumed *a priori*
85 profiles.

86 In addition to column amounts, backscattered radiances can also provide important
87 information about the height of an SO_2 layer. Conceptually, a change in altitude of an SO_2 plume
88 alters the number of backscattered photons going through the layer. If a plume is high in the
89 atmosphere, more photons that are scattered below the layer pass through the absorbing SO_2
90 plume. This results in larger SO_2 absorption structures in the measured radiance spectra,
91 especially in the 310-320 nm range where Rayleigh scattering is dominant. Relative to the SO_2
92 amount, obtaining a fast retrieval of the height of a volcanic plume presents a greater challenge.
93 Until recently, retrieval techniques have involved a direct spectral fitting approach that use BU
94 measurements in conjunction with extensive forward radiative transfer modeling. For instance,
95 the Iterative Spectral Fitting (ISF) algorithm (Yang et al., 2009) for OMI was utilized to
96 determine the altitude of SO_2 layer by adjusting the height while minimizing the differences
97 between measured radiances and forward RT calculations. Another study has utilized an optimal
98 estimation algorithm along with the VLIDORT radiative transfer (RT) model to retrieve SO_2



99 density and plume height from the GOME-2 instrument (Nowlan et al., 2011). Sulfur dioxide
100 amounts and plume heights have also been estimated with the infrared atmospheric sounding
101 interferometer (IASI), through brightness temperature changes and relative intensities of
102 absorption lines (Clarisse et al., 2008; Clarisse et al., 2014). For these techniques, extensive
103 radiative transfer modeling is needed, in addition to a variety of assumptions including a
104 reasonable first guess for the plume altitude. Newer schemes were later developed for GOME-2
105 using the SOPHRI algorithm (Rix et al., 2012), a DOAS based technique that included
106 minimizing differences between plume height from simulated spectra and the assumed height
107 from measured spectra. This technique allowed for reasonably fast retrievals that could be used
108 in near real-time, thanks to the use of pre-calculated GOME spectra that are stored in a look up
109 table classified according to SO₂ column, SO₂ heights and other physical parameters. An even
110 faster and more efficient method for GOME-2 (Efremenko et al., 2017) and TROPOMI (Hedelt
111 et al., 2019) has made use of machine learning algorithms, specifically neural networks (NNs), to
112 develop a trained full physics inverse learning machine (FP_ILM) for retrieving SO₂ plume
113 height. This approach has shown good accuracy and speed fast enough for near-real-time
114 operations. The FP_ILM has also been used for retrieving ozone profile shapes (Xu et al., 2017)
115 and geometry-dependent Lambertian equivalent reflectivity (Loyola et al., 2020). The primary
116 advantage of this approach is the execution speed. By separating the training phase, which
117 involves large amounts of time consuming radiative transfer computations and machine learning
118 model training, from the application phase, the desired parameter can be retrieved within
119 milliseconds for a single satellite ground pixel using the inverse model. However, similar
120 methods of retrieving SO₂ layer height have not yet been implemented for OMI. Now in this
121 study, the FP_ILM has been applied to OMI to estimate SO₂ layer height from backscattered
122 earthshine radiance measurements. The retrieval was tested on four past volcanic eruption cases
123 and performance was assessed through machine learning metrics, as well as comparisons to other
124 datasets such as those from TROPOMI, IASI and CALIOP lidar instruments.

125

126

127 **2 Methodology:**

128

129 In general, the FP_ILM approach consists of two parts, the training phase and the application (or
130 operational) phase. The training phase starts with the generation of a synthetic training dataset of



131 top of the atmosphere (TOA) reflectance spectra from a radiative transfer model. This spectral
132 dataset is then used to train a Multi-Layer Perceptron Regression (MLPR) NN model to predict
133 the SO₂ layer height as an output. In the application phase, the trained inverse model is applied to
134 real OMI radiance measurements. This inverse model is optimized from the training, and the
135 predictions of SO₂ layer height based on the model are very fast as compared with the time-
136 consuming RT calculations during the training phase. The main steps of the algorithm are shown
137 in a flowchart (Figure 1) and discussed in detail in the next sections.

138

139 **2.1 Forward Radiative Transfer Model**

140

141 The first step in the training phase is to build a large data set of synthetic backscattered
142 Earthshine reflectance spectra from forward radiative transfer (RT) calculations. These
143 calculations are performed using the Linearized Discrete Ordinate Radiative Transfer (LIDORT)
144 model with the rotational Raman scattering (RRS) capability (Spurr et al., 2008). This version of
145 the model treats first-order inelastic Raman scattering in addition to all orders of elastic
146 (Rayleigh) scattering processes. Rotational Raman scattering occurs when a photon is scattered
147 at lower or higher energy levels than the incident radiation. RRS cannot be neglected; it is known
148 to be responsible for the Ring effect (Grainger and Ring 1962), which is a spectral interference
149 signature characterized by the filling-in of Fraunhofer lines and telluric-absorber features.
150 Allowing for RRS in the RT model leads to differences in calculated radiances compared to
151 those made with purely elastic scattering, as characterized by the filling-in factor. This quantity
152 is generally of the order of a few percent, consistent with estimates that 4% of the total scattering
153 in the atmospheric is inelastic (Young, 1981). Fundamentally the SO₂ layer height information
154 can be retrieved by backscattered radiance spectra because the amount of scattering occurring in
155 the overlying atmosphere is determined by the height of the volcanic SO₂ plume. This is
156 demonstrated by comparing two otherwise identical RT calculations with different SO₂ layer
157 heights (Figure 1a). At shorter wavelengths where Rayleigh scattering is stronger, there is less
158 backscattered radiance for the case with higher SO₂ plume height, particularly at shorter
159 wavelengths < 320 nm (Figure 1b). Likewise, the filling-in factor (Figure 1c) shows the
160 importance of including RRS in the RT calculations as in some cases there can be 2-3%
161 difference between the Raman and elastic calculations.



162 All LIDORT-RRS calculations in this study were performed for the 310-330 nm spectral
163 range, which captures strong SO₂ and ozone absorption features. The model is supplied with
164 ozone (Daumont et al., 1992) and SO₂ absorption (Bogumil et al., 2003) absorption cross
165 sections, atmospheric profile, ozone profile and a high resolution Fraunhofer solar irradiance
166 spectrum. The atmospheric profile has 48 layers and contains a temperature/pressure/height grid
167 from the standard US atmosphere, with an increased vertical resolution of 0.5 km below 12 km.
168 The ozone profile is determined by the total column amount, latitude zone and month as
169 specified in the TOMS V7 ozone profile climatology (Bhartia, 2002), while the SO₂ profile is
170 assumed to be a Gaussian shape with a full width half maximum (FWHM) of 2.5 km. The solar
171 spectrum is a re-gridded version of the high resolution synthetic solar reference spectrum
172 (Chance and Kurucz, 2010), originally with a spectral resolution of 0.01 nm. The re-gridded
173 version has a resolution of 0.05 nm, finer than that for OMI (0.16 nm sampling for a FWHM
174 spectral resolution of ~0.5 nm). The advantage of using this reference spectrum over the
175 instrument-measured irradiance is that only one set of calculations is needed; they can be applied
176 to multiple instruments and instrument cross track positions without utilizing unique measured
177 solar flux spectra for each situation. Using instrument-measured solar flux data can be more
178 accurate and better handles issues with instrument degradation. However, that would require the
179 inverse model to be re-trained whenever a new measured solar flux spectrum is used. Since we
180 expect the retrieval to be primarily sensitive to SO₂ absorption signatures, the radiative transfer
181 calculation was performed for a molecular atmosphere with no aerosol scattering.

182 In order to obtain a large number of different spectra, eight key physical parameters were
183 varied for the LRRS calculations. These parameters include solar zenith angle (SZA), relative
184 azimuth angle (RAA), viewing zenith angle (VZA), surface albedo, surface pressure, O₃ column
185 amount, SO₂ column amount and SO₂ layer height. The ranges of these parameters are given in
186 Table 1.

187 The number of calculations and the parameter sets for each simulation were determined through
188 a smart sampling technique (Loyola et al. 2016). A selective parameter grid with sets of
189 parameters for each simulation was established through the use of Halton sequences (Halton,
190 1962) in 8 dimensions. The calculations are continued until the moments of the output data,
191 mean and median converged across all wavelengths. In total around 200,000 calculations were
192 done to achieve sufficiently comprehensive sample size for the variation in the eight parameters



193 across all rows of OMI. This sampling was done in order to ensure that 1) each set of parameters
194 was unique and training data is diverse; and 2) that the sample size of the entire dataset is large
195 enough for the machine learning application.

196

197 **2.2 Data pre-processing**

198

199 After the RT calculations are completed, the spectra are convolved with OMI instrument slit
200 function. Since each cross-track position of OMI contains a unique slit function, the appropriate
201 function was applied based on the VZA input for that particular calculation. The VZA ranges
202 from 0-70° across all rows in the OMI swath, with the middle (nadir) rows having a VZA of
203 close to 0. For each row, only spectra within $\pm 3^\circ$ of the actual VZA were convolved with the
204 appropriate slit functions. In addition, Gaussian noise with a signal-to-noise ratio (SNR) of 1000
205 was added to the spectra. While the SNR of OMI tends to be lower (Schenkeveld et al., 2017),
206 adding too much noise can greatly decrease performance of the neural network (Table 3). At
207 SNRs of less than 500, the performance starts to increasingly degrade. Between 1000 and 500
208 SNR, there is an increase of around 0.1 km in RMSE. However, adding some degree of noise is
209 necessary to account for errors satellite instrument measurements.

210 Next, principal component analysis (PCA) was applied to the spectral dataset for each
211 row, in order to extract the most significant features of the spectra, and to reduce dimensionality.
212 Since each convolved sample consists of 142 wavelength points, the dimensionality of this
213 problem becomes very large. However, PCA transforms each sample to a set of weights based on
214 8 principal components (PCs). These principal components explain 99.998% of the variance in
215 the synthetic dataset (Figure 1A). Including additional PCs does not add any significant value to
216 the retrieval and may even lead to overfitting. Prior to starting the machine learning process, the
217 dataset is split into a training subset (90%) and a testing subset (10%). The training subset is used
218 for the neural network learning, while the testing subset only deployed verifying the performance
219 of the network to predict the output.

220

221 **2.3 Machine Learning using a Neural Network**

222

223 The 8 PCs, and selected parameters including the SZA, RAA, VZA, surface pressure and
224 surface albedo were used as input for training a MLPR, which is sometimes referred to as a deep
225 neural network. The output layer of the NN contains the effective SO₂ layer height. Column



226 amounts of SO₂ and O₃ were not included in the training or in the application stage because of
227 the large dependency of column amounts on SO₂ layer height and due to biases in OMI ozone
228 retrieval in the presence of the enhanced SO₂ plume, respectively. To improve stability, the
229 inputs (PC weights, SZA, VZA, etc.) and output (effective SO₂ height) are scaled between -0.9
230 and 0.9 according to the minimum and maximum of each input variable prior to input into the
231 NN. In a NN, the input and output layers are connected by hidden layers containing neurons
232 (also known as nodes). Each neuron is connected to others by a series of weights, by means of
233 which the input data is passed to the next level as a weighted sum of all inputs. The “tanh”
234 (hyperbolic tangent) activation function is applied at the hidden layers to further increase
235 stability in the NN. Inside the neural network, the Adam optimizer with a stochastic gradient
236 descent algorithm (Kingman et al., 2014) is used to minimize the loss function, in this case the
237 mean squared error (MSE) between the result of each iteration and the actual SO₂ layer height
238 used to generate the synthetic spectral sample. With each iteration, the partial derivative of the
239 MSE with respect to each node is calculated; this is used to update the weights. The training of a
240 NN progresses by cycling through iterations of the entire training dataset, called epochs, until the
241 training and validation MSE is minimized and there is no improvement to be obtained from
242 further training.

243 While there is a lot of flexibility in the setup of NN parameters, considerable trial and
244 error is needed to determine the best configuration that optimizes performance. The final
245 configuration of the NN in this study includes 2 hidden layers with 20 and 10 nodes in the first
246 and second layer, respectively. This was determined mostly through testing and analyzing the
247 performance of the NN with respect to both the synthetic test data set and real satellite
248 measurements. For this study, the training was done separately for each OMI row due to the
249 different VZAs and slit functions between rows; however, the configuration of the NN was kept
250 constant between rows. The only difference in the training is the number of training epochs
251 conducted for each row before the solution becomes optimal for that row. With this NN
252 configuration, the number of epochs was in the 200-300 range for all rows. The final trained
253 version of the NN, the inverse operator, contains the optimal weights needed to predict the SO₂
254 layer height from an input of separate test data.

255

256 **2.4 Application to satellite measurements**



257 In the application phase of the retrieval, the inverse operator is applied to OMI radiance
258 spectra, resulting in a predicted SO₂ layer height for each ground pixel in the OMI swath. For
259 this the OMI L1B Geolocated Earthshine radiance dataset is used. Since OMI only provides
260 absolute radiances, these data were normalized with respect to the same solar flux spectrum as
261 used in the generation of the synthetic spectra. In other words, the measured input becomes the
262 fraction of backscattered radiance to the incoming solar irradiance (i.e., reflectance spectrum).
263 Prior to normalizing, the irradiance spectrum was convolved with an OMI slit function for the
264 particular OMI row and orbit. The output is a predicted SO₂ layer height based on the input of a
265 radiance spectra and associated parameters, including VZA, SZA, RAA, surface albedo and
266 surface pressure, for a single OMI pixel. The irradiance spectrum is convolved with the
267 appropriate OMI slit function in order to have consistency in wavelength points between the
268 measured radiances, synthetic radiances and irradiance of each row. To follow the same
269 procedure as was used in the training step, the PCA operator from the training phase is applied to
270 the OMI spectra to perform the dimensionality reduction and obtain a set of PC weights for each
271 sample. The other inputs are VZA, SZA, RAA, albedo and surface pressure parameters from the
272 OMI data files. As in the training phase, all inputs are scaled to the [-0.9, 0.9] range. After SO₂
273 heights are retrieved separately for each row, one height value is given for each pixel (and
274 spectral sample). The application phase of the retrieval takes only 2-3 seconds for a given row.
275 This short duration includes the application of the training phase PCA operator to OMI
276 measurements, the scaling of inputs and the deployment of the inverse operator. The whole
277 process is repeated for each row in order to get a prediction for an entire OMI swath. For some
278 rows the retrieval is unreliable due to the row anomaly, which negatively affects the quality of
279 the OMI L1B radiance data at all wavelengths and consequently L2 retrievals.

280

281 **3 Impacts of various parameters on the performance of the trained inverse model**

282

283 From the training phase, it becomes clear that the performance of the algorithm will
284 depend on several factors. As demonstrated in Fig. 3, an important factor is the SO₂ column
285 amount. Overall, the NN makes better predictions for the test data subset for SO₂ amounts > 40
286 DU. Below 40 DU, information content on the layer height to be retrieved becomes increasingly
287 small, as evidenced by large differences between predicted heights and those in the actual test set
288 (Figure 3a). Additionally, larger SO₂ loadings result in greater sensitivity between two heights,



289 as seen by comparisons of SO₂ height Jacobians for multiple amounts (Figure 2A).
290 Quantitatively, if samples with SO₂ amounts less than 40 DU are excluded, the RMSE decreases
291 from 1.48 to 1.15 km (Table 2). We can therefore expect the retrieval to produce reasonable
292 results for larger volcanic eruptions. In widely dispersed plumes where the SO₂ VCD is low, the
293 retrieval would be biased and less useful. The second major dependency is on SZA. The problem
294 here stems from the occurrence of relatively large errors in RT modeling due to shallow light
295 paths and lower OMI SNR at the higher SZAs. Reasonably accurate results are to be expected
296 only for SZA < 75°. Figure 2b shows significant differences in predicted and actual heights in
297 spectra associated with large SZAs, after removal of low VCD samples. For the final training
298 approach, it was therefore necessary to exclude spectra with large SZAs. Dependencies on other
299 physical parameters are small when compared with these two issues discussed here, although
300 there is some evidence that high surface albedo also increases error. If we remove spectra with
301 albedo > 0.6 there is a minor improvement in RMSE from 0.93 to ~0.89 km. However, even with
302 strong volcanic SO₂ signals, we can realistically expect that on average the absolute error to be at
303 least 1 km, due to inherent simplifications in the neural network retrieval approach. The errors in
304 actual retrievals using OMI data are expected to be larger (see Section 4.4).

305

306 **4. OMI SO₂ Effective Layer Height Results**

307

308 For testing the FP_ILM retrieval on OMI data, four volcanic eruption cases with sufficiently
309 strong SO₂ signals were selected (i.e. where peak SO₂ VCDs were greater than 40 DU). Each
310 case is described in detail in the following subsections. For each case, comparisons were made to
311 other satellite-derived datasets where available, for example the CALIOP lidar onboard
312 CALIPSO, the IASI SO₂ layer height retrieval (Clarisse et al., 2014), and the GOME-2
313 (Efremenko et al., 2017) and TROPOMI retrievals (Hedelt et al., 2019). It is important to note
314 that the CALIOP lidar only indicates the height of the ash plume and not the SO₂ height.
315 Although ash and SO₂ plumes are often collocated, this is not always the case, making direct
316 comparisons difficult.

317

318 **4.1 Kasatochi (2008)**

319 Kasatochi is a volcano located on the Aleutian Islands of Alaska (52.178°N, 175.508°W). It
320 underwent a series of eruptions beginning late in the day on August 7th, 2008, which injected



321 great amounts of ash and SO₂ into the stratosphere. Overall the explosion released roughly 2
322 million tons of SO₂, at the time the highest SO₂ loading since the Mt Pinatubo eruption (Yang et
323 al, 2010). SO₂ effective layer heights retrieved using the machine learning model for OMI (orbit
324 21650) on August 10th, 2008, were around 11-12 km with some portions being slightly lower
325 (Figure 4a). This is in reasonable agreement with previous SO₂ height retrievals of 9-11 km
326 which used the ISF algorithm for OMI (Yang et al., 2010). Likewise, Nowlan et al. (2011)
327 showed that the majority of the plume was around 10 km, and up to 15 km in some parts.
328 Furthermore, there is agreement with IASI (Figure 4b) and CALIOP data (Figure 4d) which
329 showed plume heights of 10-12 km and 12.5 km respectively. It is important to note that the
330 IASI overpass occurred later in the day than those for OMI and CALIPSO. Another verification
331 source we used was the GOME-2 SO₂ layer height retrieval that uses FP_ILM (Efremenko et al.,
332 2017). The study found a height of around 10 km and up to 14 km in areas of high SO₂ loading
333 for August 10th (Figure 4c). Although the OMI results agree well in general with the results of
334 these studies and datasets, the retrieval is less sensitive with respect to detecting variability in the
335 SO₂ layer height within the plume, compared to the GOME-2 case. It should be noted that the
336 GOME-2 overpass occurred earlier in the day than OMI.

337

338 **4.2 Kelud (2014)**

339 Kelud is a stratovolcano located in East Java, Indonesia (7.935°S, 112.315°E). It erupted on
340 February 13th, 2014 at 1550 UTC, in the process depositing ash in a 500 km diameter around the
341 volcano and leading to mass evacuations from nearby towns. The OMI retrieval results indicate
342 that the maximum height of the main plume was 18-19 km (Figure 5a), although other studies
343 suggest that several small layers of SO₂ and ash were located as high as 26 km (Vernier et al.,
344 2016) on the previous day. However, the SO₂ loading at that level was most likely too low for an
345 accurate retrieval using OMI radiances. CALIOP lidar detected ash plumes at around 19.5 km
346 and the IASI retrievals registered the plume at 17.5 km over the same area as that for OMI. The
347 height of the ash plume from this eruption was also estimated using Multifunctional Transport
348 Satellite (MTSAT 2) observations and transport modeling (Kristiansen et al., 2015). That study
349 found an injected height of around 17 km, which is in agreement with the OMI result, especially
350 when considering the PDF of the heights (Figure 6b). We note here that only a small portion of
351 the plume was retrieved with our algorithm, given the relatively low SO₂ VCDs and interference



352 due to the OMI row anomaly. It is promising to note that the OMI retrieval was able to identify
353 heights at the upper end of the height range used in the training phase. On the other hand, while
354 the retrieval can extrapolate to heights above 20 km, the accuracy would likely degrade due to
355 the lack of training data with heights outside of this limit.

356

357 **4.3 Calbuco (2015)**

358

359 The Calbuco eruption in April 2015 and the Kelud eruption in February 2014 are both significant
360 volcanic events that injected SO₂ plumes well above 10 km into the atmosphere. We have chosen
361 to apply the FP_ILM to these events even though they have somewhat lower SO₂ VCDs as
362 compared with those from Raikoke and Kasatochi; nevertheless, peak SO₂ columns with ~60-70
363 DU should allow reasonable accuracy in our retrievals (see section 2).

364 The Calbuco volcano is located in Chile (41.331°S, 72.609°W). The primary eruption
365 had a volcanic explosivity index (VEI) of 4 and occurred on April 22nd with little warning. The
366 primary plume ascended higher than 15 km, while plumes from smaller subsequent eruptions
367 stayed in the troposphere. The volcanic plume spread northeast in the following days, resulting in
368 flight cancellations at Uruguayan and south Brazilian airports. The OMI-retrieved SO₂ effective
369 layer heights in the area of greatest VCD was in the 15-17 km range. In the same region, IASI
370 results (Figure 5c) show similar plume heights, approximately around 15 km, although as with
371 the previous events, the overpass times of the two instruments are different. CALIOP lidar shows
372 the ash plume to at roughly 17 km (Figure 5e). Unfortunately, the overpass of CALIPSO occurs
373 over an area of OMI's swath that is affected by the row anomaly, and this makes a direct
374 comparison unfeasible. Nevertheless, the CALIPSO aerosol layer height is still comparable to
375 OMI-retrieved effective SO₂ layer heights for the portion of the plume further to the west. The
376 retrieval for OMI is consistent with the other instruments for SO₂ plumes, with the exception of
377 that part of the plume with SO₂ below 30-40 DU (see Figure 3A), for which results were not
378 plotted in Figure 5a due to lower biases.

379

380 **4.4 Raikoke (2019)**

381 The eruption of the Raikoke stratovolcano (48.2932°N, 153.254°E), located on the Kuril Islands
382 of Russia, occurred on June 21st, 2019 at 1800 UTC. A series of explosions during the eruption
383 sent large amounts of ash and SO₂ into the lower stratosphere. Maximal loadings of SO₂



384 measured by OMI and other sensors exceeded 500 DU. In the following days the plume
385 underwent dispersion and spread out over the northern Pacific Ocean and later over eastern
386 Russia. Early estimates of plume injection height for the eruption were predominantly in the 10-
387 13 km range with potentially larger heights in some areas of the plume. In Figures 7a and 7b, the
388 SO₂ effective layer heights retrieved from OMI data are shown for the Raikoke plume on June
389 23rd and June 24th respectively. The plume heights for both days are predominantly in the range
390 10-12 km, although some areas of the plume had estimated peak heights of 13-14 km. In
391 comparison, the TROPOMI results show slightly larger heights (13-14 km) for June 24th and
392 similar heights to OMI for June 23rd (Figure 7c and 7d). The IASI SO₂ height product also shows
393 fairly good agreement, with heights mainly at the 10-11 km level (Figure 7e and f). It is also
394 useful to look at a distribution of heights predicted for the domain (Figure 8) in order to get a
395 more quantitative comparison between the datasets. Based on this distribution, there is clearly a
396 1-2 km difference between the most probable heights from OMI and those from TROPOMI for
397 June 24th (Figure 8b and 8d) and slightly lower heights in the distribution for IASI. Note that
398 points with lower than 30 DU are not included in the PDFs for all sensors. The results are also
399 compared with CALIOP lidar onboard CALIPSO, which shows ash plume heights of 12-13 km
400 for both days (Figure 9a and 9b). Although there is overestimation for some OMI pixels,
401 especially for June 24th, the section of the plume with the CALIPSO flyover has similar heights
402 (around 12.5 km) to lidar-determined aerosol layer altitudes. Lastly, we note that a recent study
403 highlighted probabilistic height retrievals using the Crosstrack Infrared Sounder (CrIS) for
404 Raikoke. This study found a median height of 10-12 km across a large part of the plume,
405 however with some areas upwards of 15 km. While there are some notable differences across all
406 of the datasets, the OMI retrieval for this case falls within the general consensus of plume height
407 estimates for this volcanic event.

408

409 **4.5 Discussion of errors**

410 It is clear that predicting SO₂ layer height with FP_ILM is an efficient process, but one that is not
411 flawless in terms of accuracy. As comparisons between instruments have showed, on average
412 there were 1-2 km differences in heights, especially for the Raikoke event, although we consider
413 this to be good agreement given the estimated RMSE associated with this retrieval. In this
414 regard, the height retrieval is more likely to give a rough estimate of the SO₂ plume height rather



415 than a precise prediction. Comparison errors result from differences in instruments, forward
416 model assumptions and retrieval techniques. For instance, IASI is an IR-based instrument and its
417 retrieval does not use FP_ILM. Therefore exact agreement with IASI results is difficult to
418 achieve, although its retrievals serve as a good verification dataset. For OMI and TROPOMI,
419 which both use UV spectra and an FP_ILM algorithm approach, there are instrument differences
420 such as the pixel size, noise, radiometric accuracy and the level of degradation. TROPOMI has a
421 much finer spatial resolution compared to OMI, with footprints typically $5.5 \times 3.5 \text{ km}^2$ up to
422 maximum size $7 \times 3.5 \text{ km}^2$; TROPOMI also has enhanced SO_2 signals. Consequently,
423 TROPOMI is better able to resolve localized variations in the height throughout the plume, and
424 is likely to be more accurate overall. OMI retrievals show more or less uniform height levels
425 across the entire plume with the peak heights in areas with the best SO_2 signal. However, current
426 TROPOMI L1 data are known to have issues with instrument degradation and radiometric
427 accuracy in the UV spectral range; this could be a potential contributing factor to explain the
428 differences between the two instruments.. It is also worth mentioning that CALIOP lidar profiles
429 sometimes show disagreements with OMI retrieved heights, because CALIOP only identifies the
430 height of the ash or aerosol plume. It also offers a comparison for only a single cross section of
431 the entire plume per orbit. Overall, the consensus provided by different instrumental datasets can
432 provide a reasonable estimate for the SO_2 layer height, and if done in near real time, can aid in
433 decision making with regards to aviation safety.

434 Another source of error is present in the training phase. One difficulty here is finding the ideal
435 choice of neural network setup. With many parameters to consider, such as the number of input
436 PCs, number of layers, number of nodes, learning rate, regularization, weight initialization, etc.,
437 it is very time consuming to optimize the neural network setup. We have found a relatively
438 simply configuration that performed reasonably well with both test data and real OMI
439 measurements for all scenarios and events considered. It is difficult to improve results further
440 than $\sim 1 \text{ km}$ absolute error, even in the training phase. In the application phase, additional error
441 comes from the differences between synthetic spectra and real satellite measurements with noise
442 errors. For example, with an SNR of 500 used in training, which is a typical noise level for OMI,
443 the RMSE of the neural network prediction is around 1.25 km (Table 3). This can be considered
444 the lower limit of retrieval error when the inverse operator is used on OMI measurements.
445 Lastly, some deviations between the measured and synthetic training spectra originate from the



446 RT modeling. The calculations contain several assumptions including the SO₂ plume shape,
447 atmospheric profiles, gas profiles, and a molecular scattering atmosphere. Further testing is
448 required in order to determine if the inclusion of aerosols in RT calculations would improve the
449 algorithm performance.

450

451 **5 Conclusion**

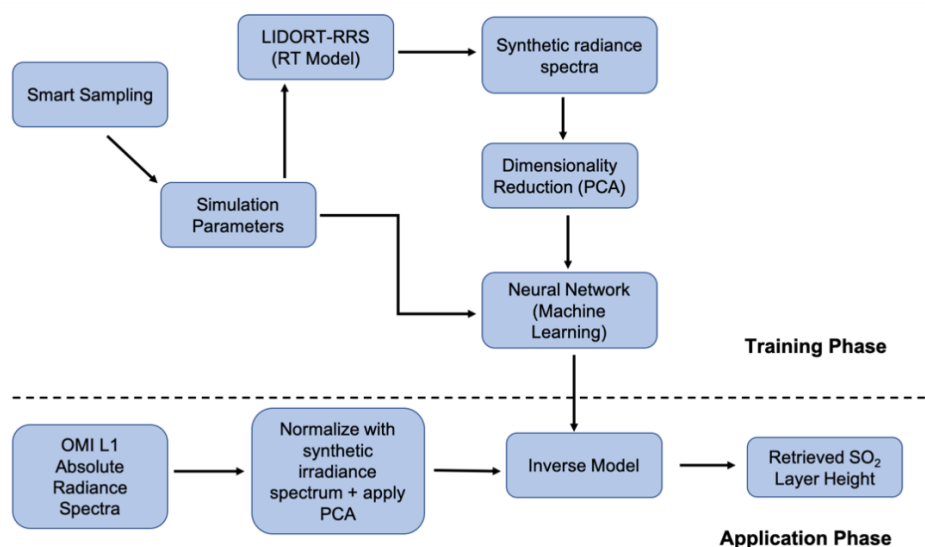
452

453 In this study we have introduced a new algorithm for OMI retrievals of the volcanic SO₂
454 effective layer height from UV earthshine radiances. This algorithm is based on an existing
455 FP_ILM method which combines a computationally time-consuming training phase with full
456 radiative transfer model simulations and a machine learning approach to develop a fast inverse
457 model for the extraction of plume height information from radiance spectra. Fast performance
458 means that the algorithm can be considered for operational deployment, given that the retrieval
459 of a SO₂ layer height prediction from the inverse model takes only a matter of milliseconds for a
460 single OMI ground pixel. For the training, a synthetic dataset of earthshine radiance spectra were
461 created with the LIDORT-RRS RT model for a variety of conditions based on choices of 8
462 physical parameters determined with smart sampling techniques. A dimensionality reduction was
463 performed through PCA in order to reduce the complexity of the problem and to separate those
464 features that best capture the great majority of variance of the dataset; 8 principal components
465 were sufficient for this purpose. Dimensionally-reduced data together with the associated
466 parameters were used to train a double hidden-layer neural network to predict SO₂ plume height
467 from any given input data. The PCA from the training phase and the inverse operator resulting
468 from the optimal NN framework were then applied to real satellite radiance spectra and
469 parameters to get retrieved values of SO₂ plume heights for several volcanic eruption events.

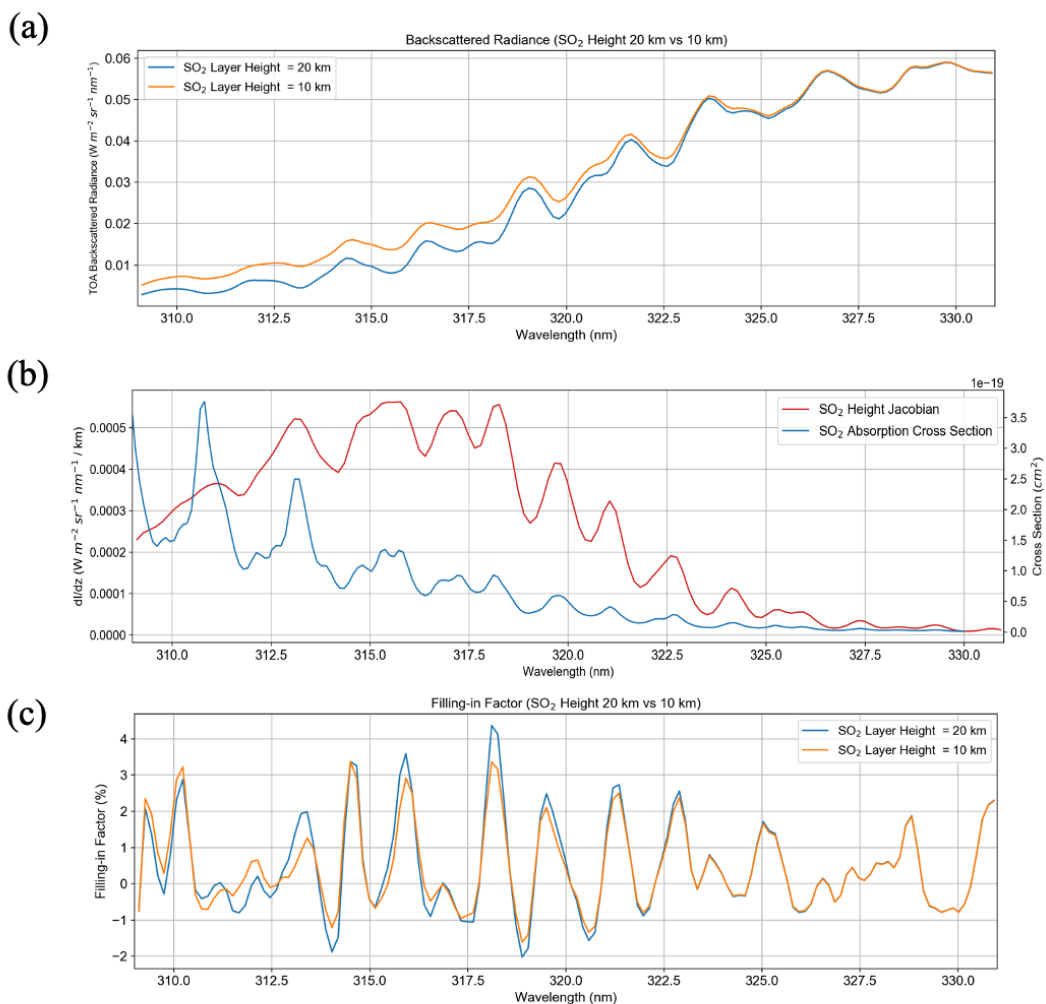
470 Through comparisons with CALIPSO lidar overpasses, TROPOMI and IASI retrievals, it
471 was shown that the retrieval for OMI can estimate reasonable SO₂ layer height for all the events
472 considered, with absolute errors of up to 1.5 km. These results can give an indication on
473 approximate plume heights achieved during medium- to large-scale eruptions, which can lead to
474 important decisions in aviation hazard mitigation. For all events treated in this study, there was
475 general agreement with CALIOP lidar, although locations of the CALIPSO flight path for the
476 Kelud and Calbuco cases were unable to be retrieved due to OMI row anomaly issues.



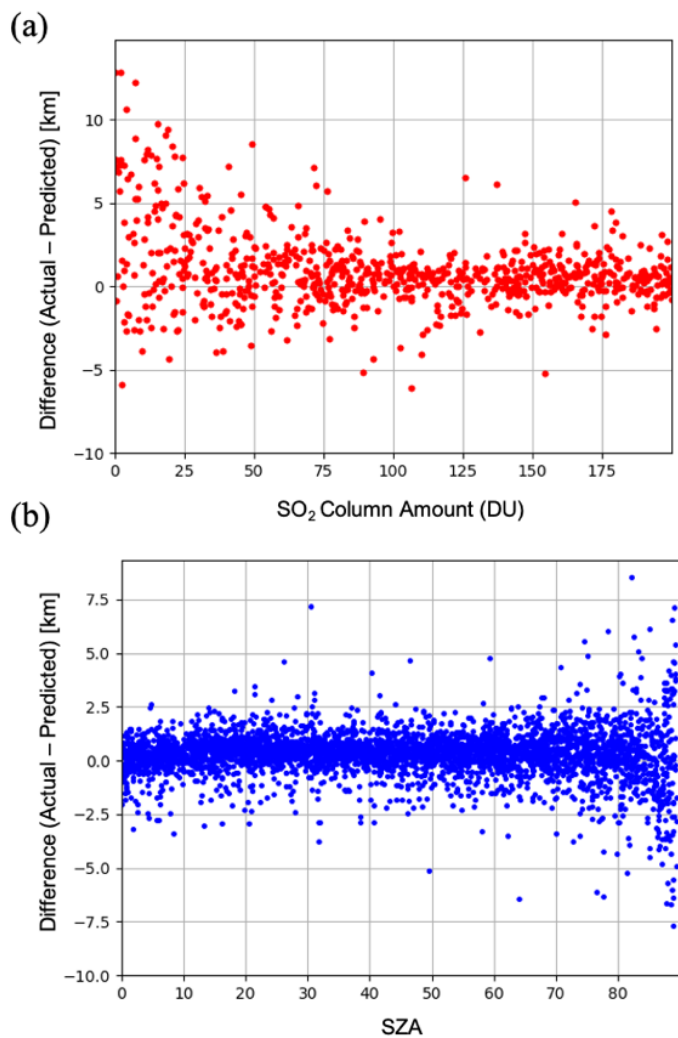
477 Uncertainties and error sources in using this approach which open up possibilities for
478 future work in improving the accuracy and robustness of this method. One assumption that was
479 made is that ash and sulfur dioxide plumes are mostly collocated when using CALIPSO as a
480 source to verify the plume height. Although this is often true, dispersion of the plume in the days
481 following the eruption can separate the two components. Therefore, tracking these plumes
482 become challenging when using reflectance spectra alone; further analysis also may need to
483 include trajectories or wind data. Secondly, the model was trained on synthetic spectra calculated
484 for molecular atmosphere conditions in the absence of any aerosol loading. The impact of
485 including aerosols in the simulations is another subject for a follow-up study. We also intend to
486 generate data sets of synthetic spectra by using a vector RRS model to account for polarization.
487 Other future work will include extending the application of FP_ILM to the Suomi-NPP OMPS
488 instrument as well as exploring the ability to predict multiple outputs at once from this approach.



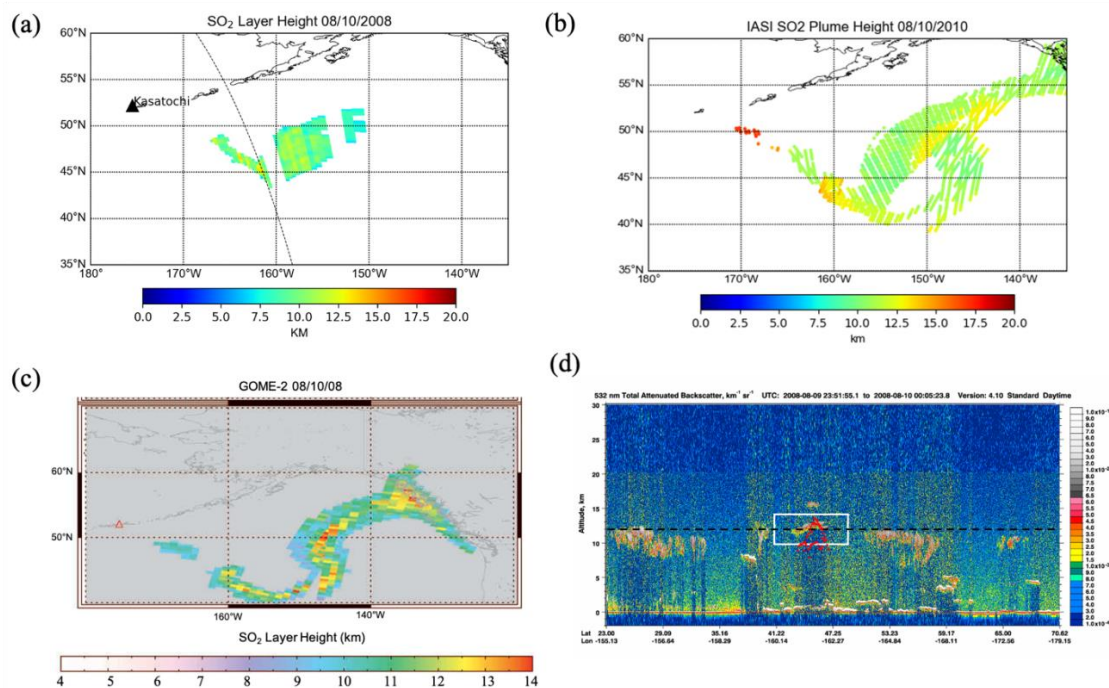
489
490 **Figure 1:** The flowchart of the FP_ILM methodology for retrieving OMI SO₂ Effective Layer Height.
491 The steps above the dashed line are part of the training phase which is done prior to incorporation of OMI
492 measurements. The application phase involves deployment of the trained model to the OMI radiance
493 measurements to obtain estimates of effective volcanic SO₂ layer heights.
494



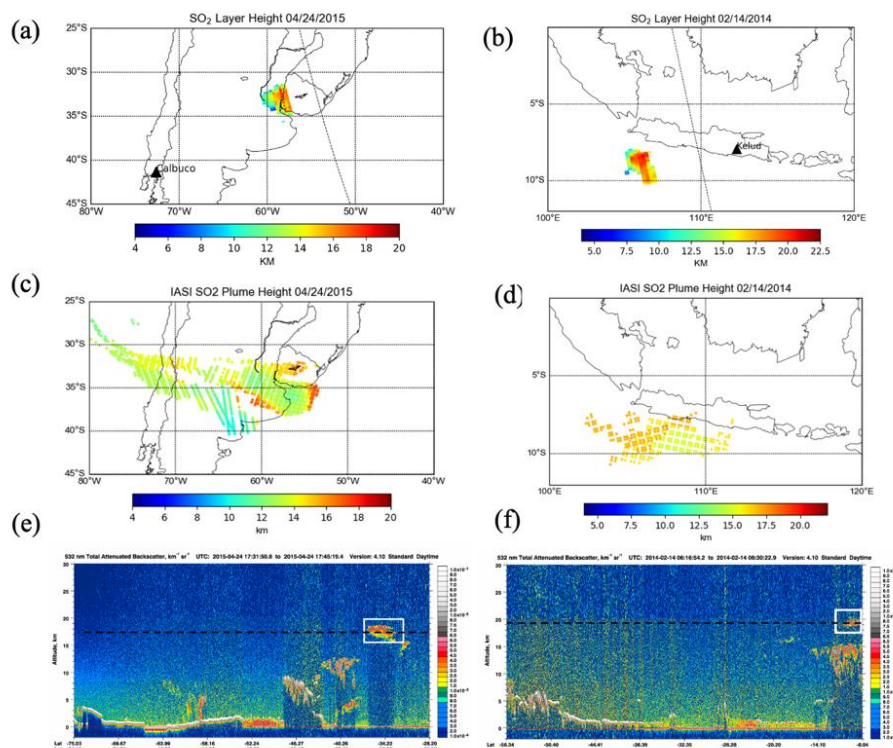
495
496 **Figure 2:** (a) Simulated top of the atmosphere (TOA) Earthshine radiances for two different SO₂ layer
497 heights (10 km and 20 km) from the LIDORT-RRS model. Also shown: (b) the SO₂ height Jacobian
498 (change in radiance per km between the two spectra) along with the absorption cross-sections of SO₂ for
499 reference; (c) the filling-in factor. The filling-in factor is defined as the difference between the total and
500 elastic-only radiance results, divided by the total radiance, expressed as a percentage. An SO₂ column
501 amount of 200 DU was used in the two calculations and all other parameters were kept constant except
502 for the SO₂ layer height.
503



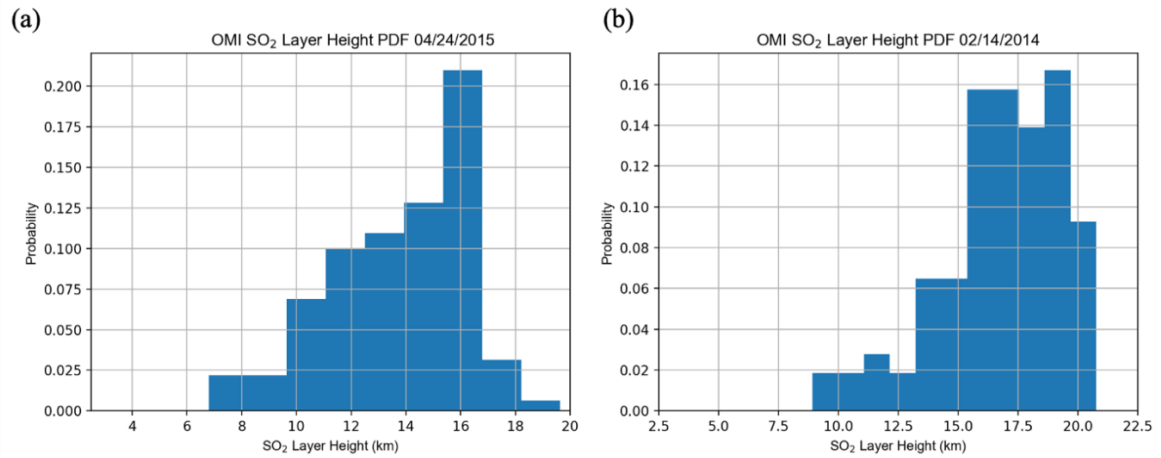
504
505 **Figure 3:** Dependence of retrieval errors on (a) SO₂ amount and (b) SZA for cases with SO₂ VCD > 40
506 DU. The error is defined as the difference between the SO₂ layer height predicted by the neural network
507 using inputs from the independent test set, and the actual height from the same samples. The test set
508 comprises 10% of the original spectral dataset withheld from training the neural network. The plots show
509 that the retrieval error is mostly within +/- 2.5 km for SZA < 70, but increases significantly for large
510 SZAs.
511



512
513 **Figure 4:** Comparison between the volcanic plume heights from (a) OMI, (b) IASI, (c) GOME-2
514 and (d) CALIOP lidar 532-nm attenuated backscatter, for the 2008 Kasatochi eruption . The
515 white rectangle in (d) shows the area of the volcanic plume on the vertical profile. The GOME-2
516 retrieval figure was obtained from Efremenko et. al 2017. The black dashed line in (a) shows the
517 CALIPSO track. Some rows of OMI in this case were affected by the row anomaly, as seen by
518 the gaps in the plume. The red dots in (d) show the OMI retrieval near the CALIPSO path.
519

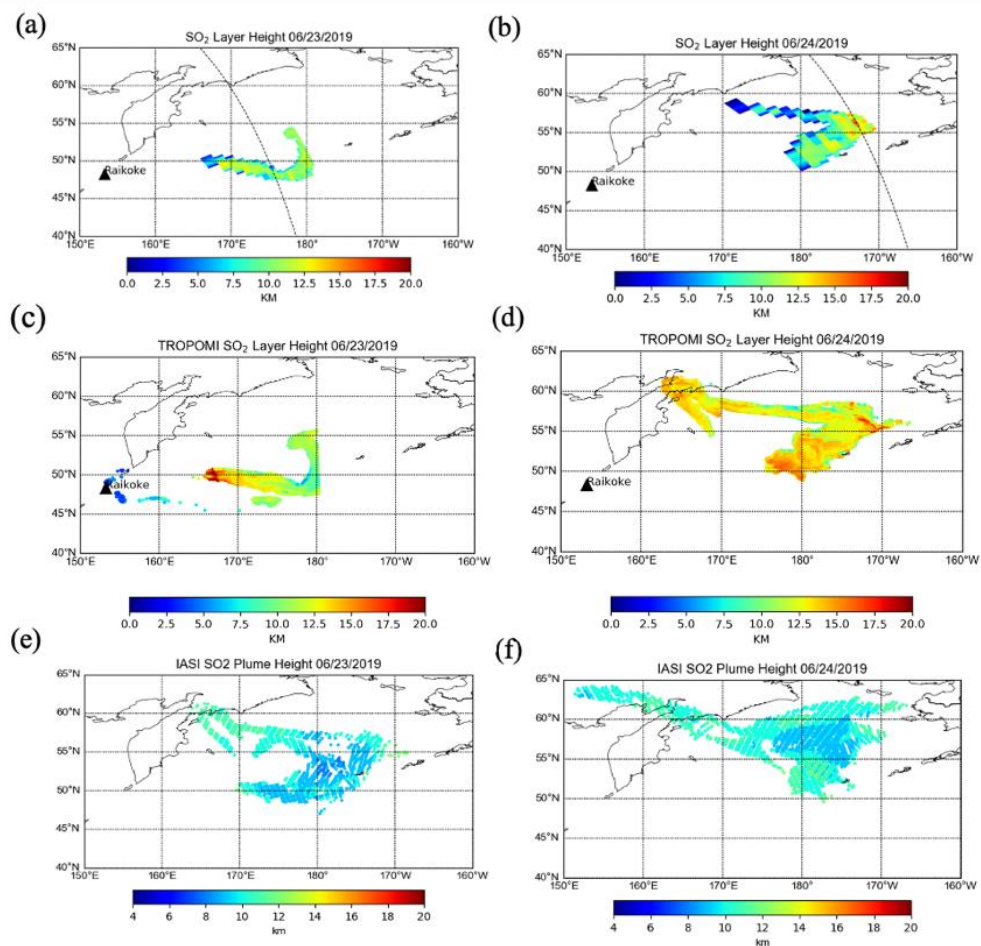


520
521 **Figure 5:** Comparisons of plume heights for the 2015 Calbuco eruption (left) and the Kelud
522 eruption (right) for OMI (a,b), IASI (c,d) and 532-nm total attenuated backscatter from the
523 CALIOP lidar (e,f). For OMI, only pixels with > 30 DU of SO₂ are shown and retrievals were
524 unavailable for some parts of the plume due to the row anomaly. The black dashed line in (a) and
525 (b) marks the CALIPSO track. The white rectangles in (e) and (f) show the location of the plume
526 in the lidar profile. Unfortunately, direct comparison with CALIPSO is not possible due to
527 obstruction by the row anomaly
528

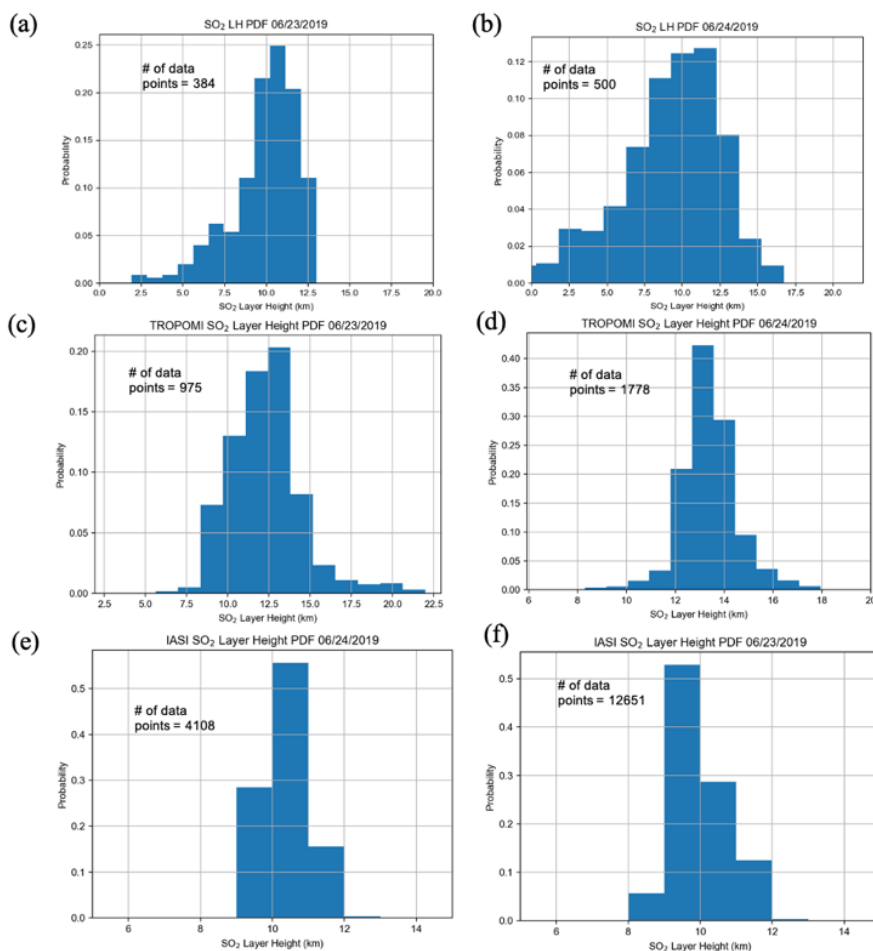


529
530
531
532

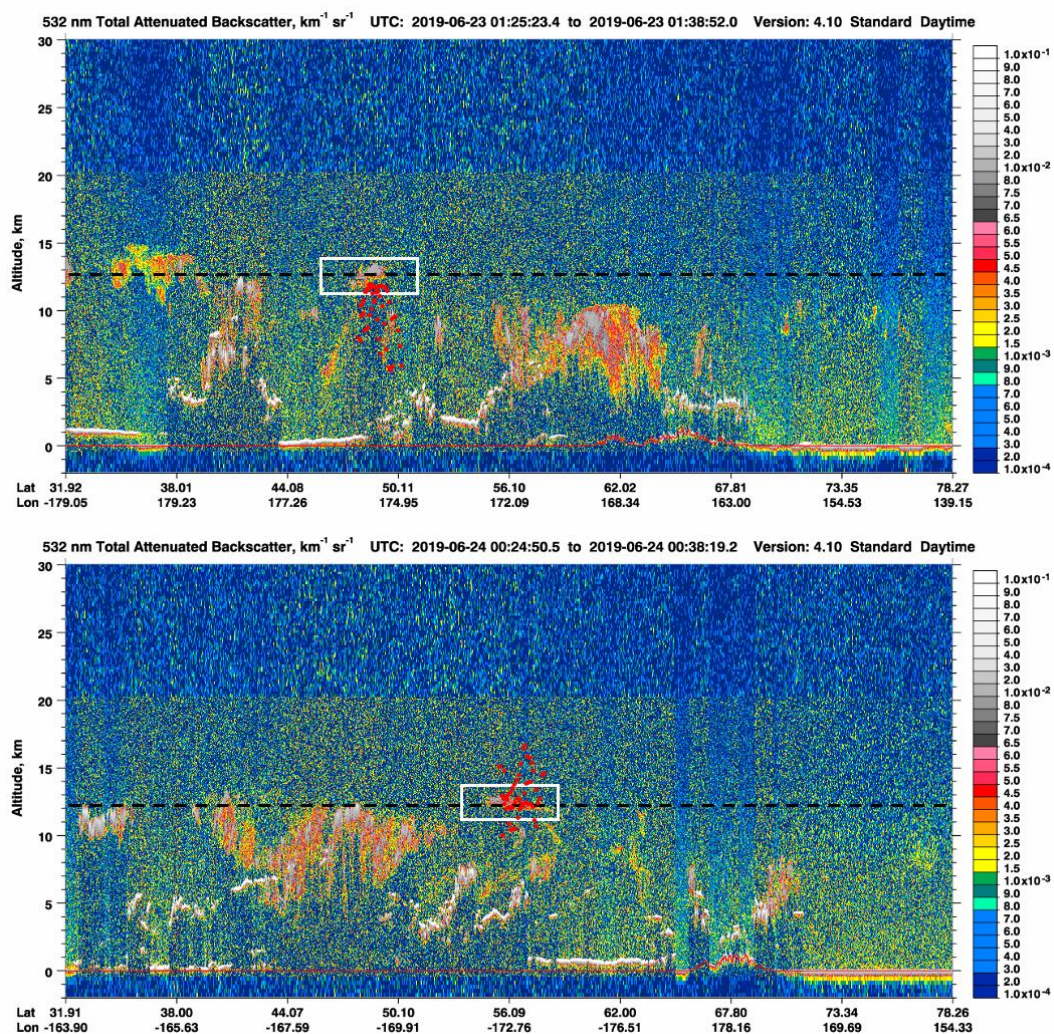
Figure 6: Probability histograms of SO₂ effective layer height retrievals for (a) the Calbuco eruption on April 24, 2015 and (b) the Kelud eruption on February 14, 2014.



533
534 **Figure 7:** The SO₂ layer height retrieval for the Raikoke eruption plume on June 23rd, 2019 (left)
535 and June 24th, 2019 (right) for the OMI (a, b), TROPOMI (c, d) and IASI (e, f) instruments. For
536 all 3 sensors, only pixels where SO₂ VCD > 30 DU are shown. Note that for IASI, the color scale
537 has been changed slightly in order to make differences within the plume more visible.
538



539
540 **Figure 8:** Probability histograms of SO₂ layer height retrievals for (a,b) OMI and (c,d),
541 TROPOMI on June 23rd, 2019 (left) and June 24th, 2019 (right) and (e,f) IASI. Only pixels with
542 SO₂ column amount greater than 30 DU are included. These plots correspond to the results
543 plotted in Figures 4a-f.
544



545
546 **Figure 9:** CALIOP lidar 532-nm attenuated backscatter for the Raikoke eruption on (a) June 23rd
547 and (b) June 24th, 2019. The white rectangle denotes the volcanic plume signature, with the black
548 dashed line symbolizing the height. Red dots show the results from the OMI retrieval along
549 CALIPSO's flight path. The flyover occurred shortly after 00:30 UTC, around the same time as
550 OMI.

551
552
553
554
555
556



557 **Table 1:** Ranges of the eight physical parameters varied in LIDORT-RRS for the synthetic
 558 spectra calculations.

Parameter	Range
Solar Zenith Angle	0-90°
Viewing Zenith Angle	0-70°
Relative Azimuth Angle	0-180°
Surface albedo	0-1
Surface pressure	250-1013.25 hPa
O ₃ VCD	225-525 DU
SO ₂ VCD	0-1000 DU
SO ₂ Layer Height	2.5-20 km

559

560

561 **Table 2:** The RMSE and the mean absolute difference of all data points in the test set under
 562 different conditions. For each condition, the appropriate points were removed and not included in
 563 calculating the errors. All cases in this table used synthetic training spectra with added SNR
 564 1000.

	All cases	SO ₂ > 20 DU	SO ₂ > 40 DU	SO ₂ > 60 DU	SZA < 75°	SO ₂ > 40 DU and SZA < 75°	Albedo < 0.6	SO ₂ > 40 DU, SZA < 75°, Albedo < 0.6
RMSE	1.487	1.216	1.150	1.109	1.281	0.931	1.524	0.895
Absolute Mean Difference (km) (Predicted – Actual)	0.910	0.834	0.803	0.782	0.795	0.697	0.895	0.667

565

566

567 **Table 3:** The RMSE and the mean absolute difference of all data points in the independent test
 568 set after adding noise as indicated by different SNR values. All other parameters and input data
 569 were kept constant. SZA < 75 degrees and SO₂ VCD > 40 DU were excluded from the test set
 570 for these comparisons.

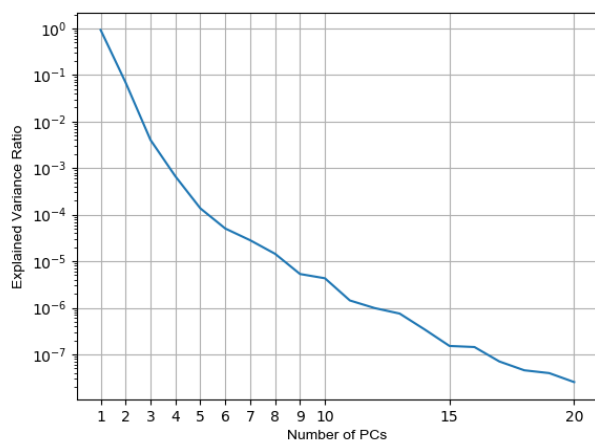
	No noise	SNR=1000	750	500	200	100
Mean Absolute Difference (y _{known} - y _{pred}) (km)	0.6805	0.697	0.7265	0.7773	0.8859	1.1825
RMSE (km)	1.093	1.150	1.176	1.2514	1.513	1.9
R-coefficient	0.989	0.985	0.984	0.981	0.973	0.957

571



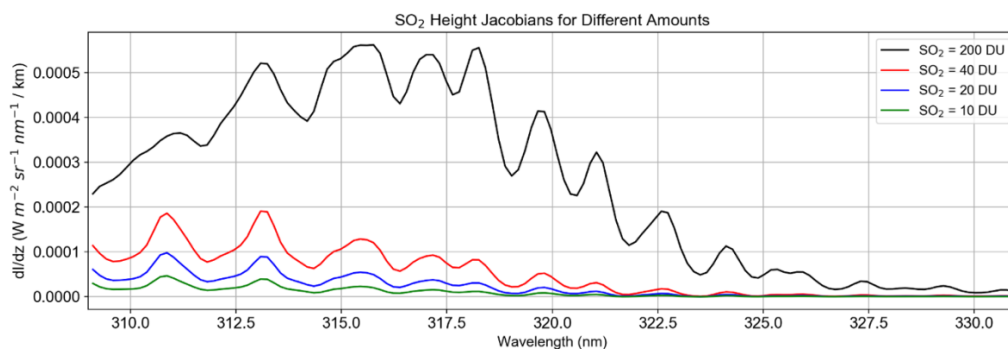
572
573
574
575

Appendix A: Supplemental Figures



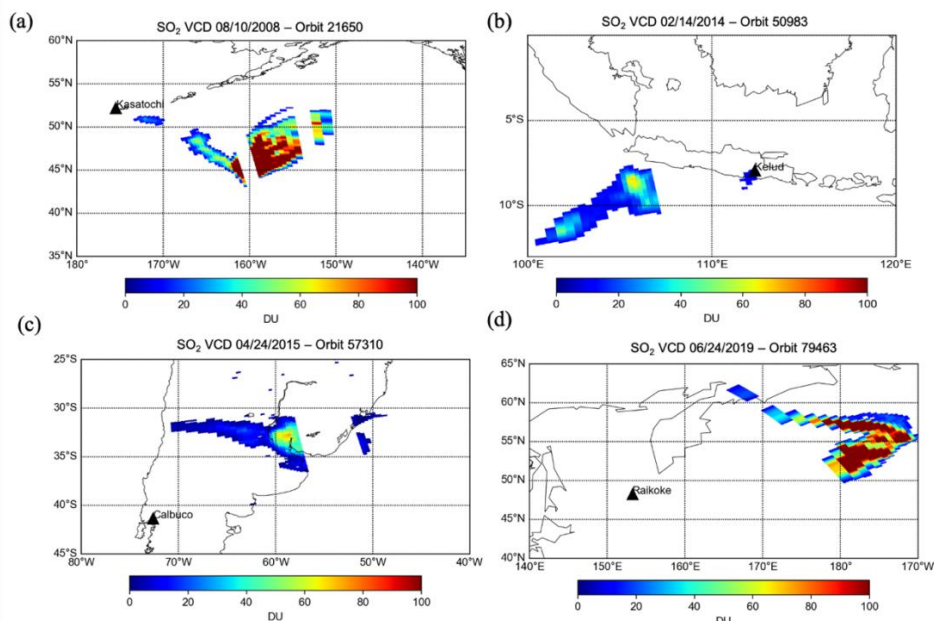
576
577
578
579

Figure 1A: Explained variance ratio as a function of the number of principal components of the spectral dataset.



580
581
582
583
584
585

Figure 2A: SO₂ Height Jacobians (dl/dz) for 4 different assumed SO₂ column amounts. The Jacobians were calculated from the difference between two radiance spectra with 10 km and 20 km SO₂ height. All other physical parameters were identical in the calculation of the spectra.



586
587 **Figure 3A:** OMI SO₂ VCD for the four volcanic cases: (a) Kasatochi on August 10th, 2008, (b)
588 Kelud on February 14th, 2014, (c) Calbuco on April 24th, 2015 and (d) Raikoke on June 24th,
589 2019. In these maps, only pixels with SO₂ > 10 DU are shown.

590
591 **Data availability.** OMI SO₂ L1 and L2 data can be accessed via the Goddard Earth Sciences Data and
592 Information Services Center (GES DISC) at <https://earthdata.nasa.gov/eosdis/daacs/gesdisc>. IASI SO₂
593 LH data is available via the IASI AERIS portal <https://iasi.aeris-data.fr/>. NASA CALIPSO data can be
594 downloaded from <https://www-calipso.larc.nasa.gov/> and images can be found at https://www-calipso.larc.nasa.gov/products/lidar/browse_images/production. TROPOMI L2 SO₂ data can be obtained
595 at <https://s5phub.copernicus.eu/dhus/#/home> while the LH is experimental and is not yet publicly
596 available online. The results of OMI SO₂ layer height retrieval presented in this study can be obtained
597 from the author by request.

598
599
600 **Author contributions.** NF wrote the manuscript and performed most computational and model work in this
601 study. The project was conceived and overseen by CL and NK. DL and PH provided the TROPOMI SO₂ LH
602 retrieval and input on the comparisons in the paper. PH also offered support relating to the machine learning
603 aspect of the study. RS is the original developer of the LIDORT-RRS code and provided related support, as
604 well as input to the relevant sections of the manuscript. RD is an advisor of NF and provided additional input
605 to the paper and was involved in project planning.

606
607



608 **Competing interests.** The authors declare that they have no conflict of interest.

609

610 **Acknowledgements.** We would like to acknowledge the NASA Earth Science Division (ESD) Aura Science
611 Team program for funding of the OMI SO₂ product development and analysis (Grant # 80NSSC17K0240).
612 OMI is a Dutch/Finish contribution to the NASA Aura mission. The OMI project is managed by the Royal
613 Meteorological Institute of the Netherlands (KNMI) and the Netherlands Space Agency (NSO).

614

615

616 **References.**

617

618 Bogumil, K., Orphal, J., Homann, T., Voigt, S., Spietz, P., Fleischmann, O. C., Vogel, A., Hartmann, M.,
619 Bovensmann, H., Frerick, J., and Burrows, J. P.: Measurements of molecular absorption spectra with the
620 SCIAMACHY pre-flight model: Instrument characterization and reference data for atmospheric remote
621 sensing in the 230–2380 nm region, *J. Photochem. Photobiol. A: Chem.* 157, 167–184,
622 doi: 10.1016/S1010-6030(03)00062-5, 2003.

623

624 Carn, S. A., A. J. Krueger, N. A. Krotkov, K. Yang, and K. Evans. “Tracking Volcanic Sulfur Dioxide
625 Clouds for Aviation Hazard Mitigation, *Natural Hazards* 51 (2): 325–343, doi:10.1007/s11069-008-9228-
626 4, 2009.

627

628 Carn, S. A., Fioletov, V. E., McLinden, C. A., Li, C., Krotkov, N. A.: *Scientific Reports*, 7, 44095,
629 doi: 10.1038/srep44095, 2017.

630

631 Chance, K., and R. L. Kurucz. An improved high-resolution solar reference spectrum for Earth’s
632 atmosphere measurements in the ultraviolet, visible, and near infrared, *J. Quant. Spectrosc. Radiat.*
633 *Transfer*, 111, 1289–1295, doi:10.1016/j.jqsrt.2010.01.036, 2010.

634

635 Clarisse, L., P. F. Coheur, A. J. Prata, D. Hurtmans, A. Razavi, T. Phulpin, J. Hadji-Lazaro, and C.
636 Clerbaux. “Tracking and Quantifying Volcanic SO₂ with IASI, the September 2007
637 Eruption at Jebel at Tair.” *Atmospheric Chemistry & Physics* 8: 7723–7734. doi:10.5194/acp-8-
638 7723-2008, 2008.

639

640 Clarisse, L., Coheur, P. F., Theys, N., Hurtmans, D., and Clerbaux, C.: The 2011 Nabro eruption, a SO₂
641 plume height analysis using IASI measurements, *Atmos. Chem. Phys.*, 14, 3095–3111,
642 <https://doi.org/10.5194/acp-14-3095-2014>, 2014.

643

644 Daumont, D., Brion, J., Charbonnier, J., and Malicet, J.: Ozone UV spectroscopy. I: Absorption cross-
645 sections at room temperature, *J. Atmos. Chem.*, 15, 145 – 155, doi:10.1007/BF00053756, 1992.

646

647 Efremenko, D. S., Loyola R., D. G., Hedelt, P., and Spurr, R. J. D.: Volcanic SO₂ plume height retrieval
648 from UV sensors using a full-physics inverse learning machine algorithm,
649 *International Journal of Remote Sensing*, 38, 1–27, <https://doi.org/10.1080/01431161.2017.1348644>,
650 2017.

651



- 652 Fioletov, V. E., McLinden, C. A., Krotkov, N., and Li, C.: Lifetimes and emissions of SO₂ from point
653 sources estimated from OMI, *Geophys. Res. Lett.*, 42, 1969-
654 1976, <https://doi.org/10.1002/2015GL063148>, 2015.
655
- 656 Guffanti, M., T. J. Casadevall, and K. Budding. Encounters of aircraft with volcanic ash clouds: A
657 compilation of known incidents, 1953-2009, Tech. rep., U. S. Geological Survey, Data Series 545, ver.
658 1.0. [Available at <http://pubs.usgs.gov/ds/545/>, 2010].
659
- 660 Halton, J. H.: On the Efficiency of Certain Quasi-Random Sequences of Points in Evaluating Multi-
661 Dimensional Integrals. *Numerical Mathematical* 2 (1), 84–90, doi:10.1007/BF01386213, 1960.
662
- 663 Hedelt, P., Efremenko, D. S., Loyola, D. G., Spurr, R., and Clarisse, L.: SO₂ Layer Height retrieval from
664 Sentinel-5 Precursor/TROPOMI using FP_ILM, *Atmos. Meas. Tech.*, 12, 5503–5517, 2019
665 <https://doi.org/10.5194/amt-12-5503-2019>, 2019
666
- 667 Lee, C., R. V. Martin, A. Van Donkelaar, R. R. Hanlim Lee, J. C. H. Dickerson, N. Krotkov, A. Richter,
668 K. Vinnikov, and J. J. Schwab.: SO₂ Emissions and Lifetimes: Estimates from Inverse Modeling Using in
669 Situ and Global, Space-Based (SCIAMACHY and OMI) Observations, *Journal of Geophysical Research:*
670 *Atmospheres* 116: (D6): n/a–n/a. D06304. doi:10.1029/2010JD014758, 2011.
671
- 672 Levelt, P. F., Van Den Oord, G. H. J., Dobber, M. R., Mälkki, A., Visser, H., De Vries, J., Stammes, P.,
673 Lundell, J. O. V., and Saari, H.: The Ozone Monitoring Instrument, *IEEE Trans. Geosci. Remote Sens.*,
674 44, 1093–1101, 2006b.
675
- 676 Li, C., Joiner, J., Krotkov, N. A., and Bhartia, P. K.: A fast and sensitive new satellite SO₂ retrieval
677 algorithm based on principal component analysis: Application to the ozone monitoring instrument,
678 *Geophys. Res. Lett.*, 40, 6314–6318, doi:10.1002/2013GL058134, 2013.
679
- 680 Li, C., Krotkov, N. A., Carn, S., Zhang, Y., Spurr, R. J. D., and Joiner, J.: New-generation NASA Aura
681 Ozone Monitoring Instrument (OMI) volcanic SO₂ dataset: algorithm description, initial results, and
682 continuation with the Suomi-NPP Ozone Mapping and Profiler Suite (OMPS), *Atmos. Meas. Tech.*, 10,
683 445–458, <https://doi.org/10.5194/amt-10-445-2017>, 2017.
684
- 685 Kristiansen, N. I., Prata, A. J., Stohl, A., and Carn, S. A.: Stratospheric volcanic ash emissions from the
686 13 February 2014 Kelut eruption, *Geophys. Res. Lett.*, 42, 588–596, doi:10.1002/2014GL062307, 2015.
687
- 688 Lee, C., R. V. Martin, A. Van Donkelaar, R. R. Hanlim Lee, J. C. H. Dickerson, N. Krotkov, A. Richter,
689 K. Vinnikov, and J. J. Schwab.: SO₂ Emissions and Lifetimes: Estimates from Inverse Modeling Using in
690 Situ and Global, Space-Based (SCIAMACHY and OMI) Observations, *Journal of Geophysical Research:*
691 *Atmospheres* 116: (D6): n/a–n/a. D06304. doi:10.1029/2010JD014758, 2011.
692
- 693 Loyola, D. G., M. Pedernana, and S. Gimeno Garcia.: Smart Sampling and Incremental
694 Function Learning for Very Large High Dimensional Data. *Neural Networks* 78: 75–87.
695 doi:10.1016/j.neunet.2015.09.001, 2016.
696
- 697 Loyola, D. G., Xu, J., Heue, K.-P., and Zimmer, W.: Applying FP_ILM to the retrieval of geometry-
698 dependent effective Lambertian equivalent reflectivity (GE_LER) daily maps from UVN satellite
699 measurements, *Atmos. Meas. Tech.*, 13, 985–999, <https://doi.org/10.5194/amt-13-985-2020>, 2020.



- 700
701 Kristiansen, N. I., Prata, A. J., Stohl, A., and Carn, S. A.: Stratospheric volcanic ash emissions from the 13
702 February 2014 Kelut eruption, *Geophys. Res. Lett.*, 42, 588–596, doi:10.1002/2014GL062307, 2015.
703
- 704 McCormick, M. P., L. W. Thomason, and C. R. Trepte.: Atmospheric Effects of the Mt Pinatubo
705 Eruption, *Nature* 373: 399–404. doi:10.1038/373399a0., 2015.
706
- 707 Nowlan, C. R., X. Liu, K. Chance, Z. Cai, T. P. Kurosu, C. Lee, and R. V. Martin.: Retrievals of Sulfur
708 Dioxide from the Global Ozone Monitoring Experiment 2 (GOME-2) Using an Optimal Estimation
709 Approach: Algorithm and Initial Validation, *Journal of Geophysical Research: Atmospheres* 116 (D18):
710 n/a–n/a. D18301. doi:10.1029/2011JD015808, 2011.
711
- 712 Rix, M., P. Valks, N. Hao, D. Loyola, H. Schlager, H. Huntrieser, A. Flemming, U. Koehler, U.
713 Schumann, and A. Inness.: Volcanic SO₂, BrO and Plume Height Estimations Using GOME-2 Satellite
714 Measurements during the Eruption of Eyjafjallajökull in May 2010, *Journal of Geophysical Research*
715 (Atmospheres) 117: D00U19. doi:10.1029/2011JD016718, 2012.
716
- 717 Schenkeveld, V. M. E., Jaross, G., Marchenko, S., Haffner, D., Kleipool, Q. L., Rozemeijer, N. C.,
718 Veefkind, J. P., and Levelt, P. F.: In-flight performance of the Ozone Monitoring Instrument, *Atmos.*
719 *Meas. Tech.*, 10, 1957–1986, https://doi.org/10.5194/amt-10-1957-2017, 2017.
720
- 721 Schmidt, A.; Witham, C.S.; Theys, N.; Richards, N.A.D.; Thordarson, T.; Szpek, K.; Feng, W.; Hort,
722 M.C.; Woolley, A.M.; Jones, A.R.; Redington, A.L.; Johnson, B.T.; Hayward, C.L.; Carslaw, K.S.:
723 Assessing hazards to aviation from sulfur dioxide emitted by explosive Icelandic eruptions. , *Journal of*
724 *Geophysical Research D: Atmospheres*, Vol. 119, Issue 24, 14180-14196, doi: 10.1002/2014JD022070,
725 2014.
726
- 727 Spurr, R., de Haan, J., van Oss, R., and Vasilkov, A.: Discreteordinate radiative transfer in a stratified
728 medium with first-order rotational Raman scattering, *J. Quant. Spectrosc. Ra.*, 109, 404–425,
729 https://doi.org/10.1016/j.jqsrt.2007.08.011, 2008.
730
- 731 Vernier, J.-P., Fairlie, T. D., Deshler, T., Natarajan, M., Knepp, T., Foster, K., Wienhold, F. G., Bedka, K.
732 M., Thomason, L., and Trepte, C.: In situ and space-based observations of the Kelud volcanic plume: The
733 persistence of ash in the lower stratosphere, *J. Geophys. Res. Atmos.*, 121, 11104–11118,
734 https://doi.org/10.1002/2016JD025344, 2016.
735
- 736 von Glasow, R., Bobrowski, N., and Kern, C.: The effects of volcanic eruptions on atmospheric
737 chemistry, *Chem. Geol.*, 263, 131–142, https://doi.org/10.1016/j.chemgeo.2008.08.020, 2009.
738
- 739 Xu, J., Schüssler, O., Loyola R., D., Romahn, F., and Doicu, A.: A novel ozone profile shape retrieval
740 using Full-Physics Inverse Learning Machine (FP_ILM)., *IEEE J. Sel. Topics Appl. Earth Observ.*
741 *Remote Sens.*, 10, 5442–5457, https://doi.org/10.1109/JSTARS.2017.2740168, 2017.
742
- 743 Yang, K., N. A. Krotkov, A. J. Krueger, S. A. Carn, P. K. Bhartia, and P. F. Levelt.: Retrieval of large
744 volcanic SO₂ columns from the Aura Ozone Monitoring Instrument: Comparison and limitations, *J.*
745 *Geophys. Res.*, 112, D24S43, doi:10.1029/2007JD008825, 2007.
746



- 747 Yang, K., X. Liu, N. A. Krotkov, A. J. Krueger, and S. A. Carn,: Estimating the altitude of volcanic sulfur
748 dioxide plumes from space borne hyper-spectral UV measurements, *Geophys. Res. Lett.*, 36, L10803,
749 doi:10.1029/2009GL038025, 2009.
750
- 751 Yang, K., P. K. Xiong Liu, N. A. Bhartia, S. A. Krotkov, E. J. Carn, A. J. Hughes, R. J. Krueger, D.
752 Spurr, and S. G. Trahan.: Direct Retrieval of Sulfur Dioxide Amount and Altitude from
753 Spaceborne Hyperspectral UV Measurements: Theory and Application, *Journal of Geophysical*
754 *Research: Atmospheres* 115: D2. doi:10.1029/2010JD013982, 2010.
755
- 756 Young, A. T.: Rayleigh Scattering. *Applications Optical* 20 (4): 533–535. doi:10.1364/
757 AO.20.000533, 1981.
758
759